SCIENCE CHINA
Physics, Mechanics & Astronomy

•Article•

May 2024 Vol. 67 No. 5: 257311
https://doi.org/10.1007/s11433-023-2327-5

# Room-temperature phonon-coupled single-photon emission in hexagonal boron nitride

Jia-Min Lai[1,2,3†], Qing-Hai Tan[1,4,5†], Feilong Song[1], Haonan Chang[1,3], Yanpei Lv[1,3], Xue-Lu Liu[1,3], Jinghua Teng[5], Weibo Gao[4], Ping-Heng Tan[1,3*], and Jun Zhang[1,3*]

[1] *State Key Laboratory of Superlattices and Microstructures, Institute of Semiconductors, Chinese Academy of Sciences, Beijing 100083, China;*
[2] *Key Laboratory of Magnetic Molecules and Magnetic Information Materials of Ministry of Education & Research Institute of Materials Science, Shanxi Normal University, Taiyuan 030000, China;*
[3] *Center of Materials Science and Optoelectronics Engineering, University of Chinese Academy of Sciences, Beijing 100049, China;*
[4] *Division of Physics and Applied Physics, School of Physical and Mathematical Sciences, Nanyang Technological University, Singapore 637371, Singapore;*
[5] *Institute of Materials Research and Engineering (IMRE), Agency for Science, Technology and Research (A*STAR), Singapore 138634, Singapore*

Received November 12, 2023; accepted January 17, 2024; published online March 8, 2024

Photon-lattice (phonon) coupling is fundamental to light-matter interaction, particularly when it reaches the quantum limit of the phonon-coupled single-photon emission, which holds great potential for quantum manipulation and quantum information transduction. Here, we report single defect state-phonon coupling in hexagonal boron nitride (hBN) at room temperature. An ultrabroad spectrum of single-photon emissions can be achieved by selecting the excitation energies. Using photoluminescence excitation spectroscopy, we observe single-phonon-assisted resonance-enhanced single-photon emission, along with multiple phonon replicas that herald the creation of phonon Fock state. We also develop a transition model to gain insight into the physical process behind the single defect state-phonon coupling. Our work sets the stage for manipulating electron-phonon coupling state with single quantum-level precision at room temperature.

**photon-phonon coupling, single-photon emission, hexagonal boron nitride**

**PACS number(s):** 63.20.Mt, 63.22.+m, 42.50.-p, 61.72.-y

**Citation:** J.-M. Lai, Q.-H. Tan, F. Song, H. Chang, Y. Lv, X.-L. Liu, J. Teng, W. Gao, P.-H. Tan, and J. Zhang, Room-temperature phonon-coupled single-photon emission in hexagonal boron nitride, Sci. China-Phys. Mech. Astron. **67**, 257311 (2024), https://doi.org/10.1007/s11433-023-2327-5

## 1 Introduction

Solid single-photon emitters play fundamental roles in quantum technologies including quantum computing, quantum communication, and quantum metrology [1]. The coupling of a single photon with other quantum entities such as atom spin and vibrational motion (i.e., phonon) holds significance for advancing quantum science and technologies [2-6]. This coupling enables not only the preparation and manipulation of the quantum state by photon counting [2], but also facilitates processes like entanglement and transduction of the quantum state. For instance, optomechanical systems have harnessed mechanical phonons to facilitate the storage and transduction of quantum states between micro-

*Corresponding authors (Ping-Heng Tan, email: phtan@semi.ac.cn; Jun Zhang, email: zhangjwill@semi.ac.cn)
†These authors contributed equally to this work.

wave and optical domains [2,7-9]. Additionally, entanglement between spatially separated vibrational states in diamonds has been achieved by mapping bulk optical phonons to Stokes and anti-Stokes scattered photons at room temperature [3,4]. Nonetheless, these studies have primarily focused on low-frequency mechanical vibrational modes or nonresonant spontaneous Raman scattering, lacking significant electronic state participation. This limitation has resulted in suboptimal scattering probabilities and low rates of photon-phonon coupling. The quantum emitters in solids provide new opportunities for exploring the single photon-phonon coupling, thanks to the bright quantum emitters and the versatility of their vibrational frequencies, spanning from acoustic to optical phonons [10,11]. In previous studies, the entanglement between a single photon and chiral phonon [12], as well as the realization of electrically tunable strong coupling between phonon and excitonic quantum emitters [13], were reported within the context of the two-dimensional material $WSe_2$. However, these achievements remain unattainable to room-temperature applications due to the necessity of cryogenic cooling for quantum emission in $WSe_2$.

Wide bandgap semiconductor hBN has emerged as an exciting platform for quantum emitters generation, controlling, and application at room temperature [14-23]. The hBN single-photon emissions exhibit a wide emission range spanning from ultraviolet to near-infrared [24-27] and tunable spectra via strain [28,29] and electric field [30,31]. In particular, the negatively charged boron vacancy centers ($V_B^-$) within hBN flakes have garnered significant attention due to their capability for spin initialization, readout, and coherent control. These attributes render them highly promising for integration into quantum technologies [18-23]. The phonon sideband of the zero phonon line (ZPL) has been observed in the photoluminescence (PL) spectra of hBN [32-38], which can be depicted by the Huang-Rhys model where the vibrational state coupled to the electronic state [39]. Therefore, hBN provides an ideal platform for studying the single defect state-phonon coupling at room temperature but remains largely unexplored.

Herein, we study the phonon-coupled single-photon emission in hBN nanoflakes. We observe broad-spectrum single-photon emissions by varying the excitation energy. The selective excitation enhancement of single-photon emission is indicative of the involvement of a single phonon in both the absorption and emission process. This can be regarded as a distinctive signature of room-temperature single photon-phonon coupling.

## 2 Material and methods

The hBN samples were prepared on $SiO_2$/Si substrate from commercial hBN flakes suspended in 50/50 ethanol/water solution (Graphene Supermarket). After dispersing 20 μL solution on $SiO_2$/Si substrate, we dried up the samples by using a warm white light, as shown in Figure 1(a). The color difference among the nanoflakes depends on the stack situation and the thickness of the nanoflakes. The experimental results depicted in Figures 1, 3, and 4 are derived from the identical position (S1) of the same single flake. Figure 2 was measured at different spots (S2-S9) of flakes on the same

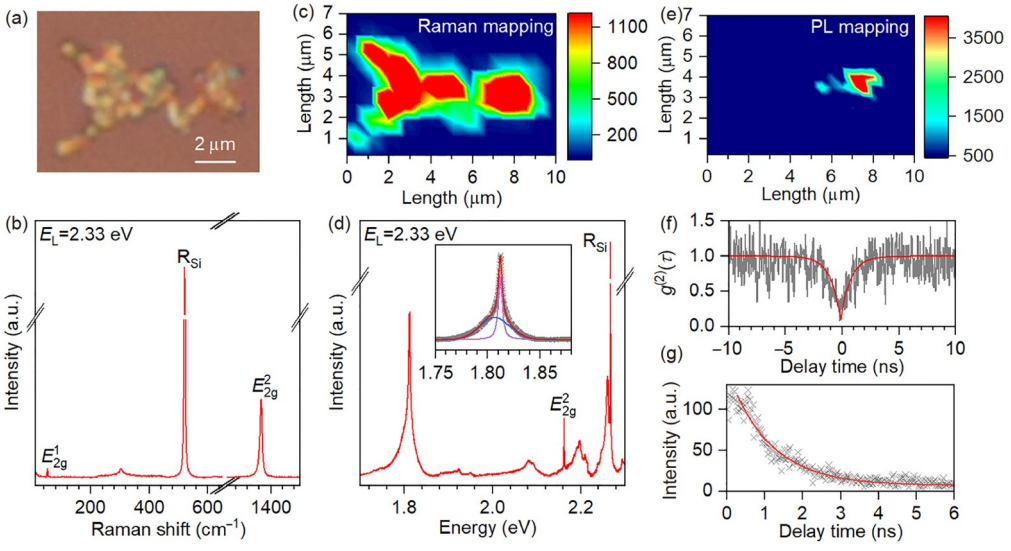


**Figure 1** (Color online) Typical optical characterization of hBN nanoflakes. (a) The optical microscopy image of hBN sample. (b) Raman spectrum of hBN sample in (a). (c) Confocal Raman mapping of $E_{2g}^2$ mode over the same area in (a). (d) PL spectrum of hBN single-photon emitter in (a) excited by 2.33 eV laser at room temperature. The inset shows the fitting results of the PL peak with two components, i.e., ZPL and phonon sideband. (e) Confocal PL mapping with a bandpass filter at 1.81 eV. (f) The second-order correlation function measurement of PL peak in (d). (g) The time-resolved intensity of PL peak in (d). The red curve was fitted by a single exponential decay function.

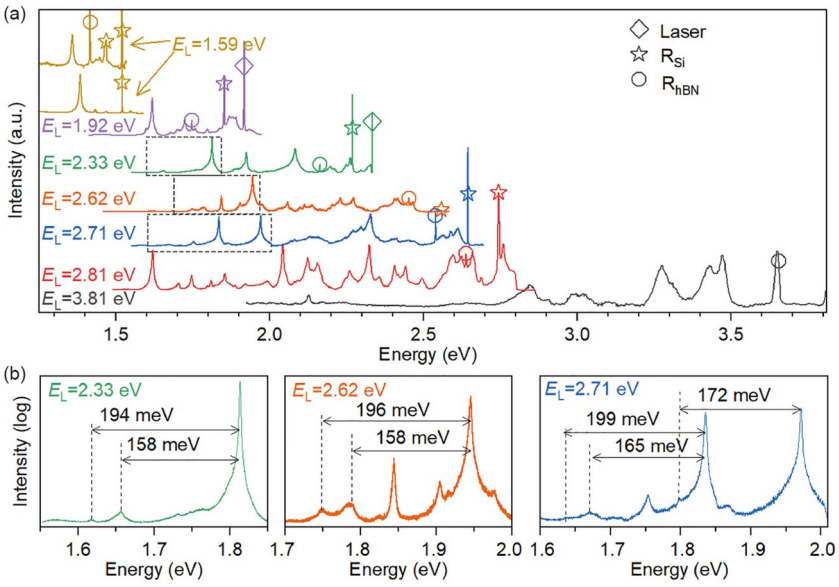


**Figure 2** (Color online) PL spectra of hBN samples with different excitation energies. The star, circle, and diamond symbols mark the Raman mode of silicon, $E^2_{2g}$ mode of hBN, and the excitation laser lines, respectively. (a) PL spectra at different spots (S2-S9) of flakes on the same substrate. The details in the dashed boxes were zoomed in (b).

substrate. All measurements were performed at room temperature.

### 2.1 Raman and PL measurement

Confocal Raman and PL spectra measurements on hBN samples were undertaken in backscattering geometry with a Jobin-Yvon HR800 and T64000 system equipped with a liquid-nitrogen-cooled charge-coupled detector. 100× objective lens (NA=0.9), 39× UV objective lens, and 1800 lines $mm^{-1}$ gratings are used for the measurements. The excitation laser ($E_L$) lines of 2.71 and 2.62 eV are from an $Ar^+$ laser; the laser line of 1.92 eV is from a $Kr^+$ laser; the laser line of 3.81 and 2.81 eV are from a He-Cd laser; the laser line of 1.94, 2.10, 2.21, 2.33, and 2.37 eV are from solid state lasers; the 3.1 eV laser is from a multimode laser.

### 2.2 PLE measurement

The PLE measurements are carried out by using a home-built confocal microscopic PLE system, where a super continuous laser source combined with a grating monochromator is used to generate the excitation light source. The moving steps for excitation wavelengths are 2 nm. The resolution of the spectrometer for PLE measurements is around 0.52 nm.

### 2.3 The second-order correlation function measurement

The second-order correlation function measurement is carried out by using a home-built Hanbury-Brown-Twiss (HBT) setup. Jobin-Yvon HR550 system with 1800 lines $mm^{-1}$ gratings was used to select the measured wavelength of the PL. Two silicon Avalanche Photo Diodes (APD) are used to count photons. The second-order correlation function was fitted by $g^{(2)}(\tau) = 1 - a e^{-|\tau|/\tau_0}$, where $a$ is the background of uncorrelated photons and $\tau_0$ is the antibunching recovery time.

## 3 Results and discussion

Figure 1(b) shows a typical Raman spectrum of the hBN sample (S1) with two Raman modes, $E^1_{2g}$ at 52 $cm^{-1}$ (full width at half maximum (FWHM) = 2.93 $cm^{-1}$) and $E^2_{2g}$ at 1366.6 $cm^{-1}$ (FWHM = 10.4 $cm^{-1}$), consistent with the result of exfoliated multilayer hBN [40]. Figure 1(c) is the corresponding confocal Raman mapping ($E^2_{2g}$ mode) of hBN, which matches the microscopic image of the hBN sample as shown in Figure 1(a).

Figure 1(d) exhibits a typical PL spectrum of hBN defect emission taken at a certain spot in Figure 1(a). Besides the Raman signals of the silicon substrate and hBN, we also observed several PL signals including a bright emitter around 1.807 eV (~684 nm), the peak closest to the $R_{Si}$ and so on. We used two peaks to fit this PL signal around 1.807 eV, i.e., a narrow one with the Lorentzian shape (FWHM ~ 4.4 meV) for the ZPL and a broader one (FWHM ~ 39 meV) with the Gaussian shape for the phonon sideband as shown in the inset of Figure 1(d). The Gaussian shape of

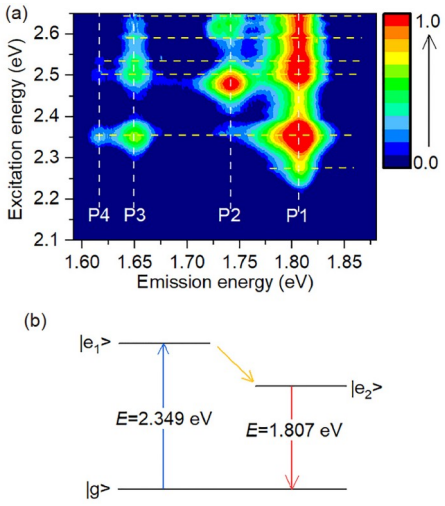


**Figure 3** (Color online) PLE mapping of hBN sample. (a) The confocal PLE mapping of single-photon emitters in hBN at room temperature (S1). The dash lines are used to guide the resonance-enhanced excitation and emission energies. (b) The three-level model of electron transition in defect state.

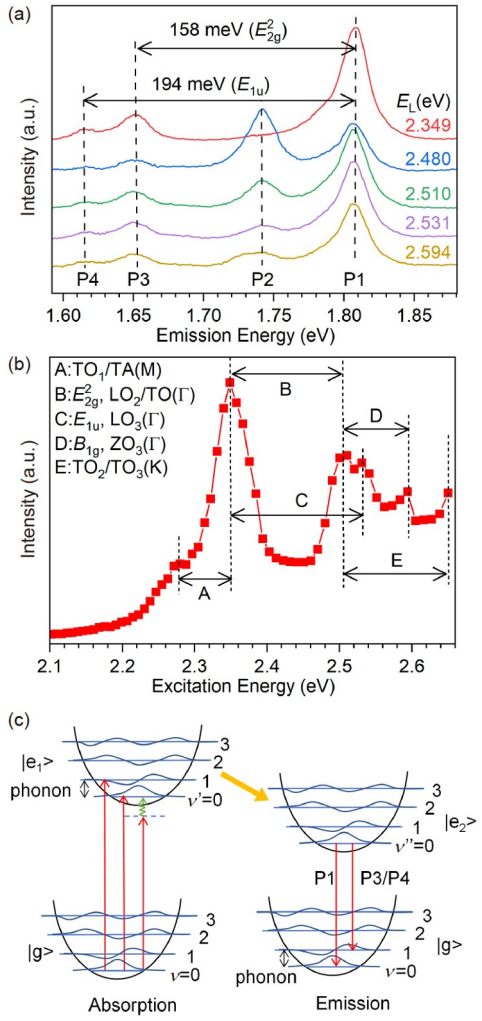


**Figure 4** (Color online) The phonon-assisted excitation and emission process of single-photon emitter in hBN. (a) The PL spectra with different excitation energies. (b) The PL intensity of the peak at 1.807 eV (P1) as a function of excitation energy. (c) The configuration coordinate diagrams of phonon-assisted excitation and emission process. $|g\rangle$ is the electronic ground state of the defect and $|e_1\rangle$ and $|e_2\rangle$ represent the excited states. $v$, $v'$, and $v''$ denote the vibration quantum numbers. The red arrows represent the electron transitions, and the yellow one is the barrierless relaxation from $|e_1\rangle$ to $|e_2\rangle$. The green curved arrow represents the phonon absorption.

the phonon sideband can be understood that here the phonons-assisted electronic transition is a discrete number of events with a Poisson distribution, and thus, approximates a Gaussian distribution [41]. The energy of the phonon sideband is 5.5 meV lower than that of ZPL, which is much lower than optical phonon energy, indicating that the phonon sideband stems from local mode oscillation or acoustic phonon mode. In contrast to the Raman mapping of the $E^2_{2g}$ mode, the PL mapping result proves the localized feature of this emission (see Figure 1(e)). The measured second-order correlation function $g^{(2)}(0)$ (~0.09) is far below 0.5 (Figure 1(f)), confirming the single-photon emission nature. The extracted lifetime ($\tau_0$) from $g^{(2)}(\tau)$ is around 1.4 ns, consistent with the time-resolved intensity result of the PL at 1.807 eV in Figure 1(g).

We measured the PL spectra at random spots (S2-S9) with distinct excitation wavelengths ranging from ultraviolet (325 nm, 3.81 eV) to near-infrared (780 nm, 1.59 eV), as shown in Figure 2(a). A series of narrow PL peaks from 357 to 912 nm were observed, consistent with previously reported results that span from 550 to 800 nm [27]. According to previous theories and experimental reports, we can deduce these PL peaks may originate from defect levels related to vacancy, carbon, and oxygen, such as $N_B$ (~2.32 eV) [42], $V_BC_N^-$ (~2.1 eV) [43], $V_NC_B$ (~2 eV) [44], $V_NN_B$ (~2.05 eV) [45], $V_B^-$ (~1.76 eV) [45,46], $O_B$ (~1.5 eV) [42]. Analogous broad spectrum emission also can be obtained at an identical spot by changing excitation energy (Figure S1, Supporting Information). The PL spectra of different spots under the same excitation energy (Figure S2, Supporting Information) show similar lineshape and energy distribution, implying that the type of defects in different spots are consistent. These results suggest ultraviolet to near-infrared defect emitters can be achieved simply by selecting special excitation wavelengths, which broaden its actual applications. We also measured the second-order correlation function of some typical peaks at different wavelengths (Figures S3 and S4, Supporting Information) and most of them show $g^{(2)}(0) < 0.5$, which confirms the single-phonon nature of these emitters. We found one common feature of these spectra is that two replicas can be found at the red-detuned sideband of ZPLs, whose energy corresponds to the optical phonon $E^2_{2g}$ (~169 meV) mode and $E_{1u}$ (~200 meV) mode of

hBN respectively, as shown in Figure 2(b). More groups of ZPL and phonon replicas in hBN spectra can be found in Figures S5 and S6. These results suggest that the phonons participate in the electron transition process in single-photon emission.

To further explore the phonon role in the single-photon emission process, we performed PLE measurements on one representative quantum emitter from S1. We found that the single-photon emission at around 1.807 eV (P1) was greatly enhanced at special excitation energies, as shown in Figure 3(a). The maximum intensity of P1 was observed at 2.349 eV excitation, which is ~542 meV above the emission energy of 1.807 eV. Based on the Franck-Condon principle and Huang-Rhys model [39], the optical transition is accompanied by the change of equilibrium atomic position called lattice relaxation. Therefore, it unavoidably leads to the energy difference between absorption and emission. However, a general lattice relaxation cannot account for such a large energy difference. Instead, the presence of a defect level around 2.349 eV appears to be a more plausible explanation. In contrast to the conventional two-level Huang-Rhys model [39], we propose a three-level model as illustrated in Figure 3(b). In this model, excited electrons at 2.349 eV initially undergo relaxation to an intermediate energy level at 1.807 eV, and subsequently revert to the ground state through radiative transition. This intermediate level might arise intrinsically from the defect or be influenced by an adjacent defect. Compared with reported calculation results [45,46], such a transition process is conceivable in $V_B^-$ defects, where the intermediate level can be attributed to the energy splitting of a doubly degenerate state originating from the Jahn-Teller effect [46]. A similar process has been proposed to explain the inconsistent polarization behavior between the absorption and emission of single-photon emitter in hBN [38].

We extracted the PL emission spectra at different excited energies, as shown in Figure 4(a). Besides P1, we observed three additional peaks located at around 1.742 eV (P2), 1.651 eV (P3), and 1.615 eV (P4). We noted that P3 and P4 manifest identical resonance profiles to that of P1. Similar to the findings in Figure 2, the energy difference between P1 and P3 (158 meV), as well as P1 and P4 (194 meV), closely align with the energies of $E_{2g}^2$ and $E_{1u}$ phonon mode, respectively. It implies that P3 and P4 are phonon replicas of ZPL (P1). This phenomenon resonates with findings reported in the context of $WSe_2$ [12,13], where the single photon-phonon interaction is observed at low temperatures. P2 belongs to another set of ZPL, which shows different resonance enhancement with excitation energies. Furthermore, by fitting the PL spectrum in Figure 4(a) (Figure S7 in Supporting Information), we obtain its Debye-Waller factor to varies from 0.67 to 0.71. Such an outcome highlights the prevalence of the ZPL in steering the emission process. The above results suggest that PLE spectroscopy provides a powerful tool to distinguish the emission of different sets of defect emitters.

The PL intensity of P1 as a function of excitation energies is shown in Figure 4(b). Compared with the phonon dispersion curve in Figure S8 and Table S1, we found that the energy differences between the resonantly enhanced peaks are close to the energy of phonon at high symmetrical points in the Brillouin zone labeled as A-E in Figure 4(b). In order to elucidate the electron transition process that occurs between defect levels, concomitant with the interplay of lattice vibrations, we present the configuration coordinate diagrams within Figure 4(c). There are three kinds of electron transition potentially involved in the absorption process: (1) Phonon-assisted upconversion, corresponding to the first enhanced absorption shown in Figure 4(b); (2) direct absorption without phonon involvement, where the transition occurs from $|g,v\rangle$ to $|e_1,v'\rangle$, with $v=v'$; (3) the absorption from $|g,v\rangle$ to $|e_1,v'\rangle$, where $v<v'$, corresponding to the blue-detuned phonon sideband in the absorption (excitation) spectrum. From the energy differences in Figure 4(b), we obtain insight into the existence of the sideband resonance absorption at frequencies corresponding to the sum of phonons, such as $E_{2g}^2 + B_{1g}$. Subsequent to the photon absorption, the excited electron state relaxes from $|e_1\rangle$ to $|e_2\rangle$ through a barrierless relaxation mechanism. Following this, the cited electrons revert to the ground state through radiative recombination, where the ZPL (P1) corresponds to $|e_2,0\rangle$ to $|g,0\rangle$ and the phonon replicas P3 and P4 correspond to $|e_2,0\rangle$ to $|g,1\rangle$. Notably, the well-resolved phonon replicas are indicative of the generation of the phonon Fock state [13].

## 4 Conclusions

In summary, we investigate the phonon-assisted resonance enhancement of single-photon emission in hBN at room temperature. We demonstrate the important role of single defect state-phonon coupling in hBN single photon emitters. The phonon signature in excitation and emission spectra can be well-explained by the three-level electronic transition model coupled with the vibrational state. By choosing the excitation energy, we achieve an ultrabroad spectrum of single-photon emission covering ultraviolet to near-infrared. Our work deepens the understanding of the phonon-coupled single-photon emission in hBN and inspires further investigation on the manipulation of the quantum state based on such coupling mechanism.

*Jun Zhang acknowledges the CAS Interdisciplinary Innovation Team, the National Natural Science Foundation of China (Grant No. 12074371), the Strategic Priority Research Program of Chinese Academy of Sciences*

*(Grant No. XDB28000000), the Research Equipment Development Project of Chinese Academy of Sciences (Grant No. YJKYYQ20210001), the Chinese Academy of Sciences-the Scientific and Technological Research council of TÜRKİYE Joint Research Projects (Grant No. 172111KYSB20210004).*

**Conflict of interest** The authors declare that they have no conflict of interest.

**Supporting Information**

The supporting information is available online at http://phys.scichina.com and https://link.springer.com. The supporting materials are published as submitted, without typesetting or editing. The responsibility for scientific accuracy and content remains entirely with the authors.


1 B. Lounis, and M. Orrit, Rep. Prog. Phys. **68**, 1129 (2005).
2 R. Riedinger, S. Hong, R. A. Norte, J. A. Slater, J. Shang, A. G. Krause, V. Anant, M. Aspelmeyer, and S. Gröblacher, Nature **530**, 313 (2016).
3 K. C. Lee, M. R. Sprague, B. J. Sussman, J. Nunn, N. K. Langford, X. M. Jin, T. Champion, P. Michelberger, K. F. Reim, D. England, D. Jaksch, and I. A. Walmsley, Science **334**, 1253 (2011).
4 S. Tarrago Velez, V. Sudhir, N. Sangouard, and C. Galland, Sci. Adv. **6**, eabb0260 (2020).
5 Q. H. Tan, Y. M. Li, J. M. Lai, Y. J. Sun, Z. Zhang, F. Song, C. Robert, X. Marie, W. Gao, P. H. Tan, and J. Zhang, Nat. Commun. **14**, 88 (2023).
6 Z. Li, J. M. Lai, and J. Zhang, J. Semicond. **44**, 011902 (2023).
7 A. Bienfait, K. J. Satzinger, Y. P. Zhong, H. S. Chang, M. H. Chou, C. R. Conner, É. Dumur, J. Grebel, G. A. Peairs, R. G. Povey, and A. N. Cleland, Science **364**, 368 (2019).
8 T. A. Palomaki, J. D. Teufel, R. W. Simmonds, and K. W. Lehnert, Science **342**, 710 (2013).
9 M. Mirhosseini, A. Sipahigil, M. Kalaee, and O. Painter, Nature **588**, 599 (2020).
10 I. Aharonovich, D. Englund, and M. Toth, Nat. Photon. **10**, 631 (2016).
11 Y. Gao, J. M. Lai, and J. Zhang, J. Semicond. **44**, 041901 (2023).
12 X. Chen, X. Lu, S. Dubey, Q. Yao, S. Liu, X. Wang, Q. Xiong, L. Zhang, and A. Srivastava, Nat. Phys. **15**, 221 (2019).
13 A. Ripin, R. Peng, X. Zhang, S. Chakravarthi, M. He, X. Xu, K. M. Fu, T. Cao, and M. Li, Nat. Nanotechnol. **18**, 1020 (2023).
14 A. Sajid, M. J. Ford, and J. R. Reimers, Rep. Prog. Phys. **83**, 044501 (2020).
15 A. Kubanek, Adv. Quantum Tech. **5**, 2200009 (2022).
16 T. T. Tran, K. Bray, M. J. Ford, M. Toth, and I. Aharonovich, Nat. Nanotech. **11**, 37 (2016).
17 A. Dietrich, M. W. Doherty, I. Aharonovich, and A. Kubanek, Phys. Rev. B **101**, 081401 (2020).
18 A. Gottscholl, M. Kianinia, V. Soltamov, S. Orlinskii, G. Mamin, C. Bradac, C. Kasper, K. Krambrock, A. Sperlich, M. Toth, I. Aharonovich, and V. Dyakonov, Nat. Mater. **19**, 540 (2020).
19 H. L. Stern, Q. Gu, J. Jarman, S. Eizagirre Barker, N. Mendelson, D. Chugh, S. Schott, H. H. Tan, H. Sirringhaus, I. Aharonovich, and M. Atatüre, Nat. Commun. **13**, 618 (2022).
20 A. Gottscholl, M. Diez, V. Soltamov, C. Kasper, D. Krauße, A. Sperlich, M. Kianinia, C. Bradac, I. Aharonovich, and V. Dyakonov, Nat. Commun. **12**, 4480 (2021).
21 A. L. Exarhos, D. A. Hopper, R. N. Patel, M. W. Doherty, and L. C. Bassett, Nat. Commun. **10**, 222 (2019).
22 X. Gao, B. Jiang, A. E. Llacsahuanga Allcca, K. Shen, M. A. Sadi, A. B. Solanki, P. Ju, Z. Xu, P. Upadhyaya, Y. P. Chen, S. A. Bhave, and T. Li, Nano Lett. **21**, 7708 (2021).
23 X. Lyu, Q. Tan, L. Wu, C. Zhang, Z. Zhang, Z. Mu, J. Zúñiga-Pérez, H. Cai, and W. Gao, Nano Lett. **22**, 6553 (2022).
24 R. Bourrellier, S. Meuret, A. Tararan, O. Stéphan, M. Kociak, L. H. G. Tizei, and A. Zobelli, Nano Lett. **16**, 4317 (2016).
25 R. Camphausen, L. Marini, S. A. Tawfik, T. T. Tran, M. J. Ford, and S. Palomba, APL Photon. **5**, 076103 (2020).
26 Q. Tan, J. M. Lai, X. L. Liu, D. Guo, Y. Xue, X. Dou, B. Q. Sun, H. X. Deng, P. H. Tan, I. Aharonovich, W. Gao, and J. Zhang, Nano Lett. **22**, 1331 (2022).
27 T. T. Tran, C. Elbadawi, D. Totonjian, C. J. Lobo, G. Grosso, H. Moon, D. R. Englund, M. J. Ford, I. Aharonovich, and M. Toth, ACS Nano **10**, 7331 (2016).
28 G. Grosso, H. Moon, B. Lienhard, S. Ali, D. K. Efetov, M. M. Furchi, P. Jarillo-Herrero, M. J. Ford, I. Aharonovich, and D. Englund, Nat. Commun. **8**, 705 (2017).
29 Y. Xue, H. Wang, Q. Tan, J. Zhang, T. Yu, K. Ding, D. Jiang, X. Dou, J. Shi, and B. Sun, ACS Nano **12**, 7127 (2018).
30 G. Noh, D. Choi, J. H. Kim, D. G. Im, Y. H. Kim, H. Seo, and J. Lee, Nano Lett. **18**, 4710 (2018).
31 N. Nikolay, N. Mendelson, N. Sadzak, F. Böhm, T. T. Tran, B. Sontheimer, I. Aharonovich, and O. Benson, Phys. Rev. Appl. **11**, 041001 (2019).
32 M. Fischer, A. Sajid, J. Iles-Smith, A. Hötger, D. I. Miakota, M. Svendsen, C. Kastl, S. Canulescu, S. Xiao, and M. Wubs, arXiv: 2209.08910.
33 O. Arı, N. Polat, V. Fırat, Ö. Çakır, and S. Ates, arXiv: 1808.10611.
34 R. N. E. Malein, P. Khatri, A. J. Ramsay, and I. J. Luxmoore, ACS Photon. **8**, 1007 (2021).
35 P. Khatri, I. J. Luxmoore, and A. J. Ramsay, Phys. Rev. B **100**, 125305 (2019).
36 Q. Wang, Q. Zhang, X. Zhao, X. Luo, C. P. Y. Wong, J. Wang, D. Wan, T. Venkatesan, S. J. Pennycook, K. P. Loh, G. Eda, and A. T. S. Wee, Nano Lett. **18**, 6898 (2018).
37 G. Grosso, H. Moon, C. J. Ciccarino, J. Flick, N. Mendelson, L. Mennel, M. Toth, I. Aharonovich, P. Narang, and D. R. Englund, ACS Photon. **7**, 1410 (2020).
38 N. R. Jungwirth, and G. D. Fuchs, Phys. Rev. Lett. **119**, 057401 (2017).
39 K. Huang, and A. Rhys, Proc. R. Soc. Lond. A **204**, 406 (1950).
40 Z. Q. Xu, C. Elbadawi, T. T. Tran, M. Kianinia, X. Li, D. Liu, T. B. Hoffman, M. Nguyen, S. Kim, J. H. Edgar, X. Wu, L. Song, S. Ali, M. Ford, M. Toth, and I. Aharonovich, Nanoscale **10**, 7957 (2018).
41 J. Friedrich, and D. Haarer, Angew. Chem. Int. Ed. Engl. **23**, 113 (1984).
42 S. Gao, H. Y. Chen, and M. Bernardi, npj Comput. Mater. **7**, 85 (2021).
43 N. Mendelson, D. Chugh, J. R. Reimers, T. S. Cheng, A. Gottscholl, H. Long, C. J. Mellor, A. Zettl, V. Dyakonov, P. H. Beton, S. V. Novikov, C. Jagadish, H. H. Tan, M. J. Ford, M. Toth, C. Bradac, and I. Aharonovich, Nat. Mater. **20**, 321 (2021).
44 A. Sajid, and K. S. Thygesen, 2D Mater. **7**, 031007 (2020).
45 M. Abdi, J. P. Chou, A. Gali, and M. B. Plenio, ACS Photon. **5**, 1967 (2018).
46 J. R. Reimers, J. Shen, M. Kianinia, C. Bradac, I. Aharonovich, M. J. Ford, and P. Piecuch, Phys. Rev. B **102**, 144105 (2020).